



Permutation entropy and complexity analysis of large-scale solar wind structures and streams

Emilia K. J. Kilpua¹, Simon Good¹, Matti Ala-Lahti^{2,1}, Adnane Osmane¹, and Venla Koikkalainen¹

¹Department of Physics, University of Helsinki, P.O. Box 64, 00014 Helsinki, Finland

²Department of Climate and Space Sciences and Engineering, University of Michigan, 2455 Hayward St., Ann Arbor, MI 48109-2143, USA

Correspondence: Emilia K. J. Kilpua (emilia.kilpua@helsinki.fi)

Received: 12 October 2023 – Discussion started: 24 October 2023

Revised: 14 March 2024 – Accepted: 15 March 2024 – Published: 27 May 2024

Abstract. In this work, we perform a statistical study of magnetic field fluctuations in the solar wind at 1 au using permutation entropy and complexity analysis and the investigation of the temporal variations of the Hurst exponents. Slow and fast wind, magnetic clouds, interplanetary coronal mass ejection (ICME)-driven sheath regions, and slow–fast stream interaction regions (SIRs) have been investigated separately. Our key finding is that there are significant differences in permutation entropy and complexity values between the solar wind types at larger timescales and little difference at small timescales. Differences become more distinct with increasing timescales, suggesting that smaller-scale turbulent features are more universal. At larger timescales, the analysis method can be used to identify localised spatial structures. We found that, except in magnetic clouds, fluctuations are largely anti-persistent and that the Hurst exponents, in particular in compressive structures (sheaths and SIRs), exhibit a clear locality. Our results show that, in all cases apart from magnetic clouds at the largest scales, solar wind fluctuations are stochastic, with the fast wind having the highest entropies and low complexities. Magnetic clouds, in turn, exhibit the lowest entropy and highest complexity, consistent with them being coherent structures in which the magnetic field components vary in an ordered manner. SIRs, slow wind and ICME sheaths are intermediate in relation to magnetic clouds and fast wind, reflecting the increasingly ordered structure. Our results also indicate that permutation entropy–complexity analysis is a useful tool for characterising the solar wind and investigating the nature of its fluctuations.

1 Introduction

The study of multi-scale magnetic field fluctuations is an active research area in space, astrophysical and laboratory plasmas. One of the few natural environments in which it is possible to study them with direct measurements is the collisionless solar wind that incessantly streams from the Sun and fills the heliosphere (e.g. Bruno and Carbone, 2013). Solar wind fluctuations are generally thought to arise from waves, turbulence and coherent structures, but many open questions regarding their nature and evolution prevail. So-called “mesoscale” solar wind structures, corresponding to structures with spatial extents of approximately 5–10 000 Mm and temporal scales ranging from ~ 10 s to 7 h near Earth’s orbit (~ 1 au), have also recently been brought to the centre of attention due to their importance in solar wind formation and evolution and their space weather impacts (e.g. Viall et al., 2021).

Outward-propagating incompressible Alfvénic fluctuations from the Sun are a common feature of fast solar wind streams (e.g. Belcher and Davis, 1971). Their non-linear interaction with inward-directed Alfvén waves generated locally in interplanetary space (e.g. Chen et al., 2020) is believed to drive a turbulent cascade of energy from large to small scales, where energy finally dissipates and heats the solar wind (Smith and Vasquez, 2021). The slow solar wind is also turbulent but with a more variable structure and a higher occurrence of coherent intermittent structures (e.g. Bruno et al., 2003; Wawrzaszek and Echim, 2021). Knowledge of the properties and nature of magnetic field fluctuations is also important for understanding large-scale heliospheric structures, such as interplanetary coronal mass ejection

tions (ICMEs) and their sheaths (Kilpua et al., 2017a) and slow–fast stream interaction regions (SIRs; e.g. Richardson, 2018), as well as for understanding how energy is transferred through their boundaries. In addition, magnetic fluctuations have an important role in the acceleration and transport of solar energetic particles (SEPs; e.g. Oughton and Engelbrecht, 2021), and highly fluctuating solar wind is also considered to be more geoeffective (e.g. Borovsky and Funsten, 2003; Osmane et al., 2015; Kilpua et al., 2017b; Telloni et al., 2021; Han et al., 2023; Dai et al., 2023).

Permutation entropy analysis (Bandt and Pompe, 2002) and Jensen–Shannon complexity analysis (Rosso et al., 2007) are powerful tools for investigating fluctuations. They have been used in wide-ranging contexts and also recently in space plasma physics studies (Weck et al., 2015; Weygand and Kivelson, 2019; Osmane et al., 2019; Good et al., 2020; Olivier et al., 2019; Kilpua et al., 2022; Raath et al., 2022). The determination of permutation entropy and Jensen–Shannon complexity is based on investigating the occurrence of permutation (or ordinal) patterns in time series. An ordinal pattern is formed by a set of subsequent values in a time series separated by time lag τ , and it thus gives information on the relation between the values forming the pattern. Varying τ allows fluctuations over multiple timescales to be investigated. The number of elements in an ordinal pattern is called the embedded dimension d , and the factorial of d gives the number of possible permutations. The frequency at which different ordinal patterns occur in a time series determines its entropy and predictability. For example, if only a few ordinal patterns are present (i.e. all other permutations have zero probability), permutation entropy is close to zero, signifying high predictability or knowledge of the underlying process. A situation in which all ordinal patterns occur with the same probability yields the maximum entropy state, signifying low predictability.

However, permutation entropy cannot yield information about the randomness of the patterns or the structural complexity of time series. Complexity is related to how far the distribution formed by all permutations in the time series is from the maximum-entropy (uniform) distribution (e.g. Zanin and Olivares, 2021). Both highly ordered cases (e.g. periodic fluctuations like sine waves) and random cases (e.g. rolling of a dice, white and pink noise) have low complexities. Note that the former case has lower entropy, and the latter is close to the maximum entropy. In between the zero- and maximum-entropy cases, complexity can have a range of values. Maximal complexities are associated with chaotic fluctuations that are structured but have lower predictability.

All those studies conducted for the solar wind using complexity and entropy analysis so far have indicated that magnetic field fluctuations are stochastic (Weck et al., 2015; Weygand and Kivelson, 2019; Good et al., 2020; Kilpua et al., 2022; Raath et al., 2022). Weck et al. (2015) analysed both laboratory plasmas and solar wind. Their study suggests that solar wind fluctuations represent fully developed

turbulence, while fluctuations in the investigated laboratory settings were weakly turbulent or not even truly turbulent. Weygand and Kivelson (2019) investigated the complexity of solar wind magnetic fluctuations in ICMEs and SIRs using both *Wind* and *Ulysses* data at distances from 1 to 5.4 au, while Raath et al. (2022) analysed *Ulysses* observations up to 0.34 au, with the focus being on periods showing low entropy. It was found that the entropy increased and complexity decreased with the increasing heliospheric distance, suggesting that solar wind fluctuations become more stochastic in nature. Good et al. (2020) and Kilpua et al. (2022) were both case studies of a slow ICME-driven sheath.

Another important characterisation of the nature of time series is to explore their memory and correlations via the Hurst exponent analysis (e.g. Ruzmaikin et al., 1994). This approach has also been used in some space physics studies, in particular to characterise geomagnetic field fluctuations and geomagnetic activity (e.g. Balasis et al., 2006, 2023; De Michelis et al., 2016). These studies have, for example, demonstrated that the scaling properties of geomagnetic fluctuation change with magnetospheric activity levels.

In this paper, we investigate the occurrence of ordinal patterns, entropy and complexity in different types of solar wind. The categories include slow and fast solar wind, ICME sheaths, SIRs, and magnetic clouds. In addition, we investigate the memory of the time series extracted from these structures by analysing their magnetic field fluctuation scaling properties with the Hurst exponent.

2 Methods and approaches

2.1 Data and event selections

Here, we use 3 s magnetic field data from the Magnetic Fields Investigation (MFI; Lepping et al., 1995) fluxgate magnetometer on board the *Wind* spacecraft (Ogilvie et al., 1995). The data are analysed in Geocentric Solar Ecliptic (GSE) coordinates. The events are gathered from 1997 to 2022, i.e. spanning over two solar cycles.

Data intervals of 12 h duration were taken from the following types of solar wind, with the number of events for each solar wind type given in parentheses: slow wind (55), fast wind (49), SIR (70), ICME-driven sheath regions (27) and magnetic clouds (74). The lower number of sheath events is explained by the requirement to have the interval duration be at least 12 h. We note that sheaths and SIRs may, in particular, have some significant variations in their properties over the interval (e.g. Kilpua et al., 2017a), but we did not separate them into sub-intervals to have durations that are as long as possible for investigation. In SIRs, the stream interface (SI) separates the cooler, denser and slower solar wind from the tenuous, hot and fast wind (e.g. Gosling et al., 1978; Richardson, 2018). In sheaths, the field and plasma close to the shock have been recently processed by the shock, while close to the

ICME leading edge, the plasma and field have evolved considerably since encountering the shock and could have been further modified by processes at the sheath–ICME boundary, e.g. field line draping. Both sheaths and SIRs are compressive structures, but a typical SIR at 1 au is not preceded by a shock (Jian et al., 2006). Here, we focus on the subset of ICMEs called magnetic clouds, which represent large-scale flux ropes ejected from the Sun (e.g. Burlaga et al., 1981; Klein and Burlaga, 1982).

The magnetic clouds were collected from the *Wind* ICME catalogue (Nieves-Chinchilla et al., 2018) and the Richardson and Cane ICME list (Richardson and Cane, 2010), the SIR times were collected from the ACE/WIND stream interaction region catalogue, and sheaths were collected from the list published by Kilpua et al. (2021). Here, we considered SIRs where the solar wind speed reached at least 650 km s^{-1} after the SIR. Fast wind intervals were defined as the periods when the average wind speed during a 12 h interval after the SIR was $> 600 \text{ km s}^{-1}$. The slow solar wind intervals were defined as the periods preceding the SIR, during which the 12 h averaged wind speed was $< 450 \text{ km s}^{-1}$.

2.2 Permutation entropy and Jensen–Shannon complexity

As discussed in Sect. 1, there are $d!$ possible permutations for the embedded dimension d . For example, if $d = 5$, there are 120 possible permutations: 12 345 (indicating that samples in the series have a monotonously ascending order from beginning to end), 13 245, 12 425, etc. If we denote the probability of permutation j to be p_j and the set of probabilities to be P , the permutation entropy according to Bandt and Pompe (2002) is defined as

$$S(P) = - \sum_{j=1}^{d!} p_j \log p_j. \quad (1)$$

From the above, we see that $S(P) = 0$ when only one permutation occurs, and it maximises when all permutations occur with equal probability. The normalised Shannon permutation entropy,

$$\mathcal{H}_S(P) = S(P) / \log d!, \quad (2)$$

is defined such that it takes values between 0 and 1, where 0 is the lowest entropy, and 1 is the maximum entropy.

The Jensen–Shannon complexity as defined by Rosso et al. (2007) is

$$C_J^S = -2 \frac{S(\frac{P+P_e}{2}) - \frac{1}{2}S(P) - \frac{1}{2}S(P_e)}{\frac{d!+1}{d!} \log(d!+1) - 2 \log(2d!) + \log d!} \mathcal{H}_S(P). \quad (3)$$

The quantity $S(\frac{P+P_e}{2}) - \frac{1}{2}S(P) - \frac{1}{2}S(P_e)$ is the Jensen–Shannon divergence, which is a measure of similarity between two probability distributions. In this case, P is the

distribution formed by the patterns in the investigated time series, and P_e is the distribution that maximises the permutation entropy, i.e. the one where all permutations occur with equal probability. As stated in Sect. 1, both the perfectly random ($P = P_e$) and perfectly ordered ($\mathcal{H}_S(P) \approx 0$) cases yield zero complexity. In general, complexity is lower the closer the distribution P is to the maximum entropy state and the lower the normalised permutation entropy $H(P)$. The highest complexity values require the repeated occurrence of certain patterns that reflect underlying chaotic processes; i.e. they occur when distribution P is far from P_e but has higher normalised entropy.

The statistical robustness has been tested for the complexity–entropy analysis. The analysed time series must be long enough so that enough permutation sequences can be extracted to allow all possible permutations to be sufficiently sampled. The commonly used robustness criteria are $N/d! > 5$ and $\sqrt{d!}/(N - (d-1)r) < 0.2$ (e.g. Osmane et al., 2019; Weygand and Kivelson, 2019), where N is the number of samples in the investigated time series, and r gives the sub-sampling rate; i.e. the time lag $\tau = r\Delta t$, where Δt is the data resolution. Here, the length of each time series is 12 h at 3 s resolution, thus giving 14 000 samples in each interval. Here, we use $d = 5$, which is similar to many previous studies of the solar wind (Weck et al., 2015; Weygand and Kivelson, 2019; Good et al., 2020). The embedded dimension of 5 gives $N/d! = 120$, and we limit our analysis to $r = 600$ ($\tau = 1800 \text{ s}$). This gives $\sqrt{d!}/(N - (d-1)r) = 0.10$, indicating that both robustness criteria are well met.

2.3 Hurst exponent

We also calculate the Hurst exponents for the investigated time series. As mentioned in the Introduction, the Hurst exponent H is used to characterise the memory and correlations in stochastic time series. We calculate here the Hurst exponent from the first-order structure function that, for a time series $x(t)$, is defined as (e.g. di Matteo, 2007; De Michelis et al., 2016; Gilmore et al., 2002; Giannattasio et al., 2022)

$$S_1(\tau) = \langle |x(t+\tau) - x(t)| \rangle \sim \tau^H. \quad (4)$$

When the scaling is linear, the Hurst exponent can be estimated as linear regression fits to $\log_{10}(\langle |x(t+\tau) - x(t)| \rangle)$ as a function of $\log_{10}(\tau)$. In practice, this means calculating auto-correlations of x with time lags τ .

The value $H \sim 0.5$ signifies an uncorrelated random walk with short memory (general Brownian motion or Brown noise), where the mean-squared distance from the starting point of the walk increases with time. Such a time series is uncorrelated in the sense that the steps in the random walk are independent of each other or, in other words, that the auto-correlation of the time series is zero. Hurst exponent values < 0.5 refer to mean-reverting time series where increases are followed by decreases and vice versa, while time series $H > 0.5$ are said to be persistent, where an increase is

followed by an increase or a decrease is followed by another decrease.

For time series that are monofractal, the Hurst exponent relates to the spectral slope α of the fluctuation power spectrum $f^{-\alpha}$ as $\alpha = 2H + 1$ (Mandelbrot, 1977; di Matteo, 2007). This gives $H = 0.33$ for the Kolmogorov scaling, with spectral slope $\alpha = -5/3$ (Kolmogorov, 1941), and $H = 0.25$ for the Iroshnikov–Kraichnan scaling, with spectral slope $\alpha = -3/2$ (Iroshnikov, 1964; Kraichnan, 1965). There are, however, indications that solar wind time series are generally multi-fractal in nature (e.g. Marsch and Tu, 1997; Bruno, 2019; Gomes et al., 2023; Kilpua et al., 2020), and, therefore, this relation needs to be considered with caution.

As the scaling properties of the time series may not be constant, we use a local Hurst exponent estimated by sliding a time window through the analysed time series, as was done, for example, by De Michelis et al. (2016). The authors note that the window length needs to be at least 10 times larger than the maximum scale investigated. Here, we use a window width of 18 000 s (5 h), sliding in 30 min steps through each 12 h time series, allowing us to have the largest investigated time lag be set as 1800 s (30 min). The Hurst exponents are determined over 360 s (6 min) wide time lag intervals ($\Delta\tau$) in $\tau = 30$ s steps from 60 to 1740 s. These 360 s intervals are stepped forward in 90 s steps. The events where the standard error in the fitting was > 0.05 were removed from the analysis. We note, however, that there are now drastic differences in the results when all exponents are included (data not shown), suggesting that removal of the points does not have a strong influence.

3 Result

3.1 Examples

Examples of solar wind data during each solar wind type are presented in Fig. 1. The data series are shown only during the analysed intervals, and boundaries such as the shock and the ICME leading edge for the sheath are thus not included in the plots. It can be seen that the magnetic cloud data series differs considerably from the other four solar wind types displayed. It exhibits smooth variations in all three of the field components and a steady magnetic field magnitude. SIRs and sheaths exhibit the most variations in their properties and in the field magnitude. The fast wind interval is characterised by the uniform presence of large-amplitude fluctuations that are typically taken to represent anti-sunward-propagating Alfvén waves. The three bottom panels of Fig. 1 show white noise, pink noise and Brownian motion. These data series were created using the same sample length as the solar wind series above, i.e. 14 400 samples. The white and pink noise were created using publicly available Python codes. White noise is a maximally random series where different frequencies have equal intensities. Its power spectral density is constant and

gives a spectral slope of zero; i.e. for a $f^{-\alpha}$ power law, $\alpha = 0$. Pink noise is associated with the f^{-1} spectrum; compared to white noise, it has relatively more power at low frequencies than at high frequencies. In the solar wind, the f^{-1} spectral range is often interpreted as the “energy-containing” range, found at large scales where energy is believed to be injected into the system before cascading down the turbulent inertial range (e.g. Bruno and Carbone, 2013).

In the bottom panel, Brownian motion is shown for three values of the Hurst exponent. The Hurst exponent H is used to characterise the memory and correlations in the time series (e.g. Ruzmaikin et al., 1994). The exponent $H = 0.5$ describes the Brownian random walk (also called brown noise or classical Brownian motion) where the mean-squared distance from the starting point of the walk increases with time. Such a time series is uncorrelated in the sense that the steps in the random walk are independent of each other or, in other words, that the auto-correlation of the time series is zero.

When $H \neq 0.5$, the process is called fractional Brownian motion (fBm). In such cases, the increments in the random walk are not independent. The light-brown curve in Fig. 1 shows the case with $H = 0.8$. When $H > 0.5$, the time series is said to be persistent and exhibits long-term memory or long auto-correlation. The distance from the starting point in the random walk increases faster than in the case of classical Brownian motion. The increasing (decreasing) value is followed by an increase (decrease), and the entropy is lower. The dark-brown curve shows the case where $H = 0.2$. A time series with Hurst exponent < 0.5 is said to be mean-reverting or anti-persistent; i.e. an increase (decrease) is followed by a decrease (increase). Such a short-memory series is unpredictable and has higher entropy and lower complexity when compared to brown noise or the case with $H > 0.5$. Now the distance from the starting point increases slower than that for classical Brownian motion. A visual inspection of the solar wind time series reveals that the slow solar wind and magnetic cloud time series are the most consistent with the larger Hurst exponents, while the other intervals appear to be more like the short-memory fBm and pink noise.

3.2 Ordinal patterns

We first investigate the occurrence of ordinal patterns in time series of the three GSE magnetic field components sampled across all events within the different solar wind categories. Figure 2 shows the distributions of the median occurrence of permutations for three time lags $\tau = 180, 600$ and 1800 s (corresponding to subsampling rates $r = 60, 300$ and 900) and for $d = 5$; i.e. each ordinal pattern has five elements. Note that a fixed number has been added to all curves except for “magnetic cloud” to aid comparison between different categories (see the figure caption for details). The shaded areas show the interquartile ranges. For the smallest timescales shown ($\tau = 180$ s), both the lower and upper quartiles are

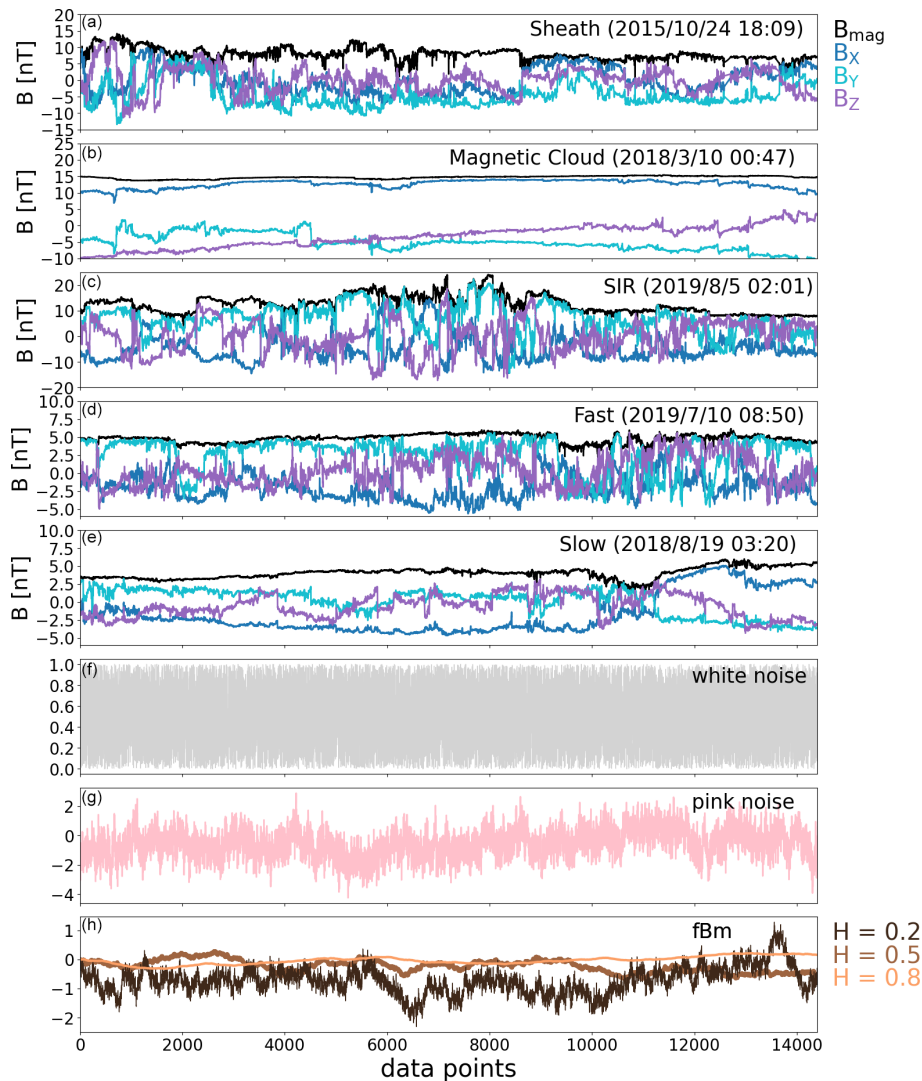


Figure 1. Example intervals. The top five panels show the interplanetary magnetic field components in GSE coordinates (blue: B_X , cyan: B_Y , purple: B_Z) and the field magnitude (black). The data shown are 3 s data from the *Wind* spacecraft. The three bottom panels show white noise, pink noise and Brownian motion for the same sample size (14 400 samples) as the solar wind intervals. Brownian motion is shown for three different values of the Hurst exponent: $H = 0.2$ (persistent), $H = 0.5$ (classical Brownian motion) and $H = 0.8$ (trend-reverting).

very close to the median, while for the largest timescales, $\tau = 1800$ s values are more spread.

A clear trend visible in Fig. 2 is that the permutations with several monotonically increasing and decreasing numbers (12 345, 54 321, 12 354, 21 345, etc.) are most abundant, in particular for $\tau = 180$ s, for all investigated solar wind categories and magnetic field components. As the timescale increases, such peaks become weaker for the fast wind in particular. For the magnetic clouds and also for sheaths, the peaks become even more pronounced. Another striking feature in Fig. 2 is that, for $\tau = 180$ and 900 s in particular, the peaks and dips in the occurrence of permutations are highly correlated across all investigated solar wind categories and magnetic field components. The magnetic cloud category

stands out as the one having certain permutations also dominating at the largest scales.

3.3 Entropy and complexity of fluctuations

The (normalised) permutation entropy and complexity as a function of time lag τ (i.e. $r\Delta t$) are investigated in the two top panels of Fig. 3 for $d = 5$. The time τ is increased from 60 s ($r = 20$) to 1800 s ($r = 600$) in steps of 60 s ($r = 20$). The uncertainty ranges indicated in the complexity panels are estimated from the average permutation occupation number $\sqrt{d!/(N - (d - 1)r)}$ (e.g. Weygand and Kivelson, 2019; Good et al., 2020). The uncertainties increase with increasing time lag (i.e. with increasing r) as the total number of permu-

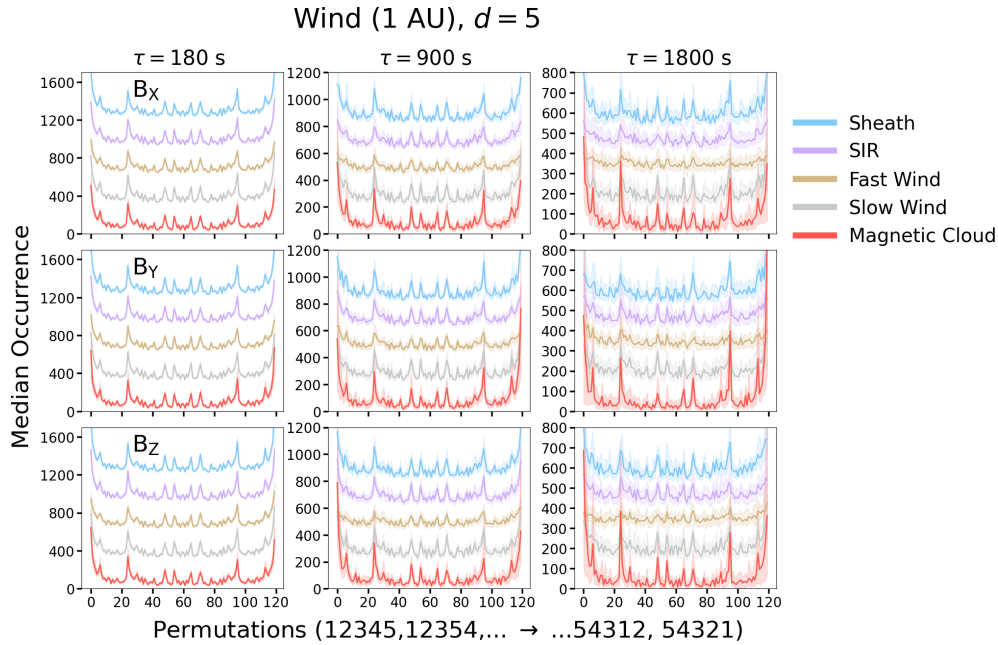


Figure 2. Median occurrence of permutations observed in different solar wind categories for $d = 5$ for $\tau = 180, 900$ and 1800 s, i.e. for subsampling rates $r = 60, 300$ and 600 , for the three GSE magnetic field components. Note that all curves except the magnetic cloud curves have been shifted upwards by a fixed amount of 300 for $\tau = 180$ s, 200 for $\tau = 900$ s and 130 for $\tau = 1800$ s to aid in the comparison. Shaded areas show the interquartile range.

tations extracted from the time series decreases slightly with decreasing τ (r).

The top panels of Fig. 3 show that the entropies in the fast-wind, slow-wind, sheath and SIR categories show no or very weak dependencies on τ , with entropy being weakly reduced at larger τ in some components for the latter three categories. The magnetic cloud entropy, in contrast, shows a significant τ dependence, falling strongly in all three components at large τ . For the fast wind the entropy in turn consistently increases very weakly with τ before flattening. These trends are similar for all magnetic field components. The key difference is that, for magnetic clouds, B_Y and B_Z components decrease to considerably lower entropies than B_X at the largest τ . The values of entropy also differ between different solar wind categories at $\tau \gtrsim 300$ s. The fast wind consistently has the highest entropy, and magnetic clouds consistently have the lowest entropy across all three components, with the other categories being at intermediate values.

The complexity (second-row panels) broadly mirrors the entropy trends: with increasing τ , complexity is approximately invariant in the fast wind; increases weakly in SIRs, sheaths and slow wind; and increases significantly in magnetic clouds. The relatively low entropy and high complexity in the magnetic clouds at large τ reflect their coherent, ordered structure at large scales, while the high entropy and low complexity of the fast wind reflect its unstructured, stochastic nature at all of the scales we have considered here. Again, the key difference between the components is for magnetic

clouds. For the B_Y and B_Z components, the complexity increases to larger values than for B_X at the largest τ .

The third row of Fig. 3 shows scatter plots of the average entropy and complexity values for the different solar wind categories. The time lags are shown from $\tau = 60$ s (lighter and smaller circles) to 1800 s (darker and larger circles). The bottom row of Fig. 3 magnifies the high-entropy, low-complexity corner of the plots. The curves are shown for fBm, with the Hurst exponent running from 0.05 to 0.75 in steps of 0.05, and for both time lags $\tau = 60$ and $\tau = 1800$ s (subsampling rates $r = 20$ and $r = 600$). These plots show that the averaged values from the solar wind time series closely follow the fBm curves. In general, the averaged data points move towards the higher Hurst exponent ends of the fBm curves with increasing τ (increasing subsampling rates). The clearest exception is the fast wind. For the fast wind, data points are clustered at the bottom-right corner, and its data points exhibit higher entropies and lower complexities at the smaller τ . We also note that, for most cases, the data points for larger time lags are a bit above the fBm curve, indicating a higher complexity.

3.4 Complexity–entropy map

In this section, we investigate how the solar wind data series are placed onto the complexity–entropy plane, where the vertical axis shows complexity, and the horizontal axis shows entropy (see, e.g. Weck et al., 2015; Weygand and Kivelson, 2019). Highly stochastic fluctuations are represented by

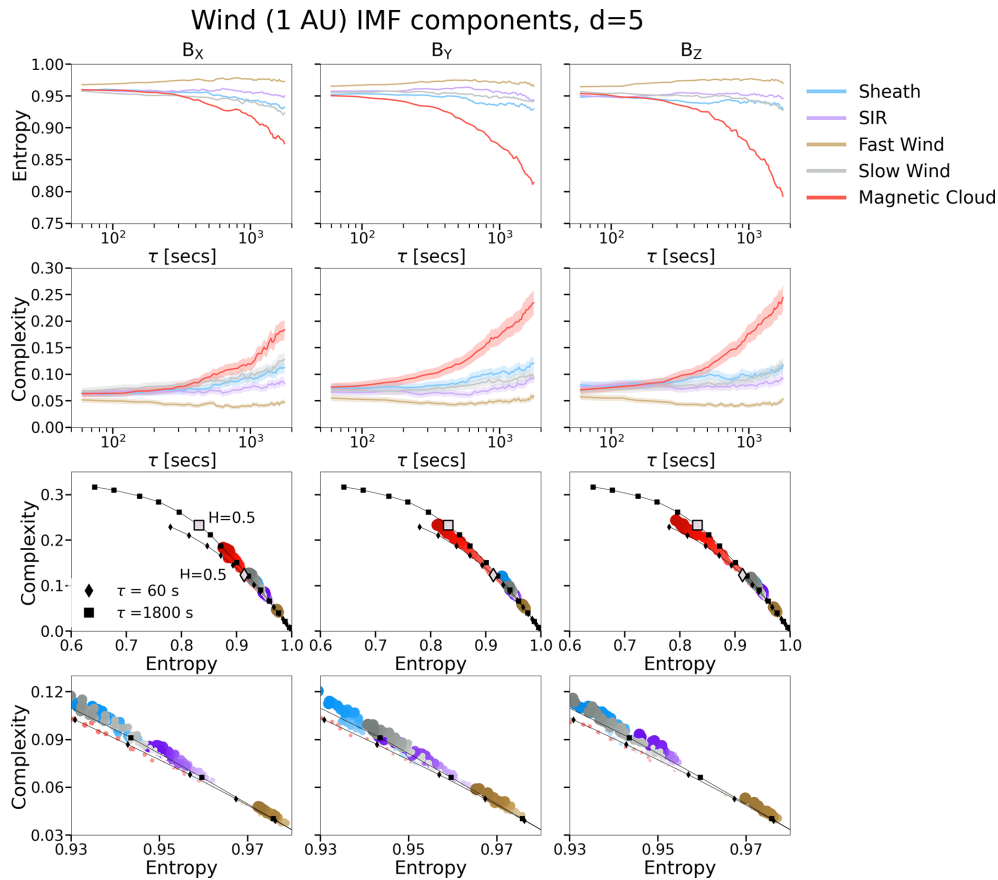


Figure 3. Entropy (first-row panels) and complexity (second-row panels) as a function of τ for $d = 5$ for the GSE magnetic field components (panels left to right) in the different solar wind categories (colour-coded lines). Shaded areas in the bottom panels give the uncertainty ranges estimated using the permutation occupation number approach. The third- and fourth-row panels give scatter plots of average entropy and complexity for the different solar wind categories from $\tau = 60$ to 1800 s in steps of 20 s. Time lag increases with the size and darkness of the marker circles. Two curves with black diamonds and squares show fractional Brownian motion for subsampling rates $r = 20$ and $r = 600$, respectively. The grey square and diamond markers show the curves at Hurst exponent 0.5.

white and pink noise, which appear in the very bottom-right part of the plane, with entropy ~ 1 and complexity ~ 0 . Chaotic fluctuations have entropies between ~ 0.45 – 0.70 and complexities close to the maximum complexity curve (e.g. Zanin and Olivares, 2021). Periodic fluctuations (e.g. sinusoidal functions) would fall onto the lower-left part of the plane (not shown). They have low entropies of ~ 0 – 0.50 , and, while their complexities follow the maximum complexity curve, they do not attain the peak values. Given that differences between the GSE components were found to be relatively small in Sect. 3.2, here we choose to investigate B_Z only. B_Z is also the IMF component that is of the most interest for geoeffectivity (e.g. Kilpua et al., 2017b).

Figure 4 shows the distribution of computed values for different solar wind categories in the complexity–entropy plane for time lags $\tau = 180, 900$ and 1800 s (subsampling rates $r = 60, 300$ and 900). The dark-blue-coloured dots correspond to $\tau = 180$ s, grey dots correspond to $\tau = 900$ s, and the yellow dots correspond to $\tau = 1800$ s. The fBm points

for varying Hurst exponents are also shown in the figure for three investigated time lags and subsampling rates. The two black curves show the minimum and maximum complexity curves.

Magnetic clouds clearly exhibit the widest spread of data points in the complexity–entropy map. Their entropies reach the $H = 0.8$ markers and complexities of about 0.35. While data points for $\tau = 180$ s fall onto the fBm curve, a significant fraction of data points deviate from the fBm curve for time lags $\tau = 900$ and 1800 s. There is a clear trend that the data points move to lower entropies and higher complexities with the increasing time lag.

The fast-wind data points are, in turn, clustered at the lower-right part of the map, with the majority of them having entropies $\gtrsim 0.96$. For the slow wind and compressive structures (i.e. sheaths and SIRs), the lowest entropy values are ~ 0.8 . For other solar wind structures the organisation with τ is less clear than for magnetic clouds. While the data points furthest along the fBm curves are solely related to the largest

time lag $\tau = 1800$ s, in the lower-right corner there is a mixture of data points from all included time lags. In particular, for the fast wind and SIRs, this region is occupied with data points related to $\tau = 900$ and $\tau = 1800$ s.

3.5 Hurst exponent

The results of the Hurst exponent analysis are presented in Figs. 5 and 6 for the B_z component. The values are averaged across all events. The top panels of Fig. 5 show the colour maps of the Hurst exponent values as a function of the midpoint of the sliding-window $\Delta\tau$ range and the time from the start of the 12 h interval in bins as described above. The bottom panels of Fig. 5 show the percentage of the events when the standard error related to the fitting was > 0.05 , i.e. the percentage of the removed points. At the smallest scales, the fitting was good for all events, while at the largest scales up to $\sim 10\%$ had the standard error exceeding our threshold.

The different solar wind types have some clear differences in their Hurst exponent values and show temporal variations in time. The fast solar wind clearly has the lowest Hurst exponents from the investigated solar wind types, being ~ 0.20 or below at the front part of the fast stream at the larger scales. The low Hurst exponents indicate anti-persistent properties of the time series. In addition, the beginning of the sheaths, i.e. the region following the shock, and the end part of the SIRs also have low Hurst exponents. In terms of spectral slopes, values below the Kraichnan scaling (corresponding to $H < 0.25$) could stem from the inclusion of the part of the f^{-1} range, but as discussed in Sect. 2.3, the connection between the Hurst exponent and spectral slopes is affected by solar wind typically exhibiting multifractality. The inclusion of part of the f^{-1} range could also explain the fact that fast wind had the largest percentage of cases with poor fit. The low-frequency break point for the fast wind occurs at relatively high frequencies (at 1 au frequencies corresponding to a few hours), while in the slow solar wind, it is found only when long-enough (several days) time series are used (e.g. Bruno and Carbone, 2013; Chen et al., 2020).

The largest average Hurst exponent values are found for the sheaths and, in particular, for magnetic clouds. For magnetic clouds, the largest exponents are clustered at the largest $\Delta\tau$ and at the middle part of the cloud. For sheath, SIR and fast wind, the Hurst exponents tend to decrease with increasing timescales, while for the magnetic clouds, the trend is indeed the opposite. Figure 5 also reveals a strong locality in Hurst exponents for sheaths and SIRs. Sheaths clearly have the largest Hurst exponents at their end parts, i.e. closer to the leading edge of the driving ICME ejecta than to the shock. For SIRs, the Hurst exponents, in turn, get smaller close to the end part of the SIR. The slow wind, in turn, does not show any obvious trends in the Hurst exponents with timescale or with the investigated interval.

Probability density functions (PDFs) of the Hurst exponent for varying $\Delta\tau$ are shown in Fig. 6. Here, the PDFs

include values combined over the entirety of the 12 h intervals. Firstly, for all investigated cases, the PDFs become considerably flatter; i.e. the values are spread over a much broader range with increasing timescales. Secondly, the majority of the Hurst exponent values are in the anti-persistent regime ($H < 0.5$). For the fast wind, a strong peak is present at the Hurst exponent values $H \approx 0.33$ for smaller $\Delta\tau$; this moves to $H \approx 0.25$ with increasing $\Delta\tau$. In the case of monofractal time series, these peaks represent the Kolmogorov and Kraichnan scalings, respectively.

The slow-wind PDFs peak at slightly larger Hurst exponent values and have heavier tails towards large values than for the fast wind. The relative order in the Hurst exponents for the fast and slow wind is in agreement with their spectral slopes from several previous studies (e.g. Teodorescu et al., 2015; Borovsky et al., 2019; Yordanova et al., 2009); i.e. the fast wind is known to have, in general, shallower slopes than the slow wind. The sheath and SIR distributions are overall quite similar to the slow-wind PDFs. For magnetic clouds, the PDFs extend considerably to the persistent $H > 0.5$ regime, particularly so for the larger $\Delta\tau$.

4 Discussion

We first studied the occurrence of ordinal patterns, i.e. permutations in different solar wind types (fast and slow wind, magnetic clouds, SIRs, and ICME-driven sheaths). The ordinal patterns were constructed here from the set of five data points separated by a time lag τ (subsampling rate r). We found that their occurrences were very similar, in particular for timescales of 180 and 900 s, with certain permutations showing distinct peaks for all solar wind types. The consistent occurrence of certain permutations suggests the presence of coherent structures or waves in the data.

At the smallest scale of 180 s, for all investigated solar wind types, we also found a clear dominance of ordinal patterns, with a small change between the subsequent values, i.e. implying the absence of sudden and large changes in the magnetic field. Such peaks persisted for sheaths and slow wind, as well as for magnetic clouds, in particular for the largest time lag included in the analysis (1800 s, i.e. 30 min), while for the fast wind, peaks already got less dominant at the time lag 900 s. The reason is that, at the largest timescales, magnetic clouds become increasingly sensitive to the coherent flux rope rotation. The persistence of peaks at large scales for sheath regions and slow wind also suggests some coherent global structuring for these solar wind types.

The entropy and complexity values between different solar wind types were found to be very similar at the smallest timescales and/or subsampling rates up to $\tau \sim 300$ s (subsampling rate $r \sim 100$). This suggests a uniformity in the physical processes operating at smaller scales, independent of the large-scale structure of the solar wind. The entropy and complexity also remained relatively stable as a function

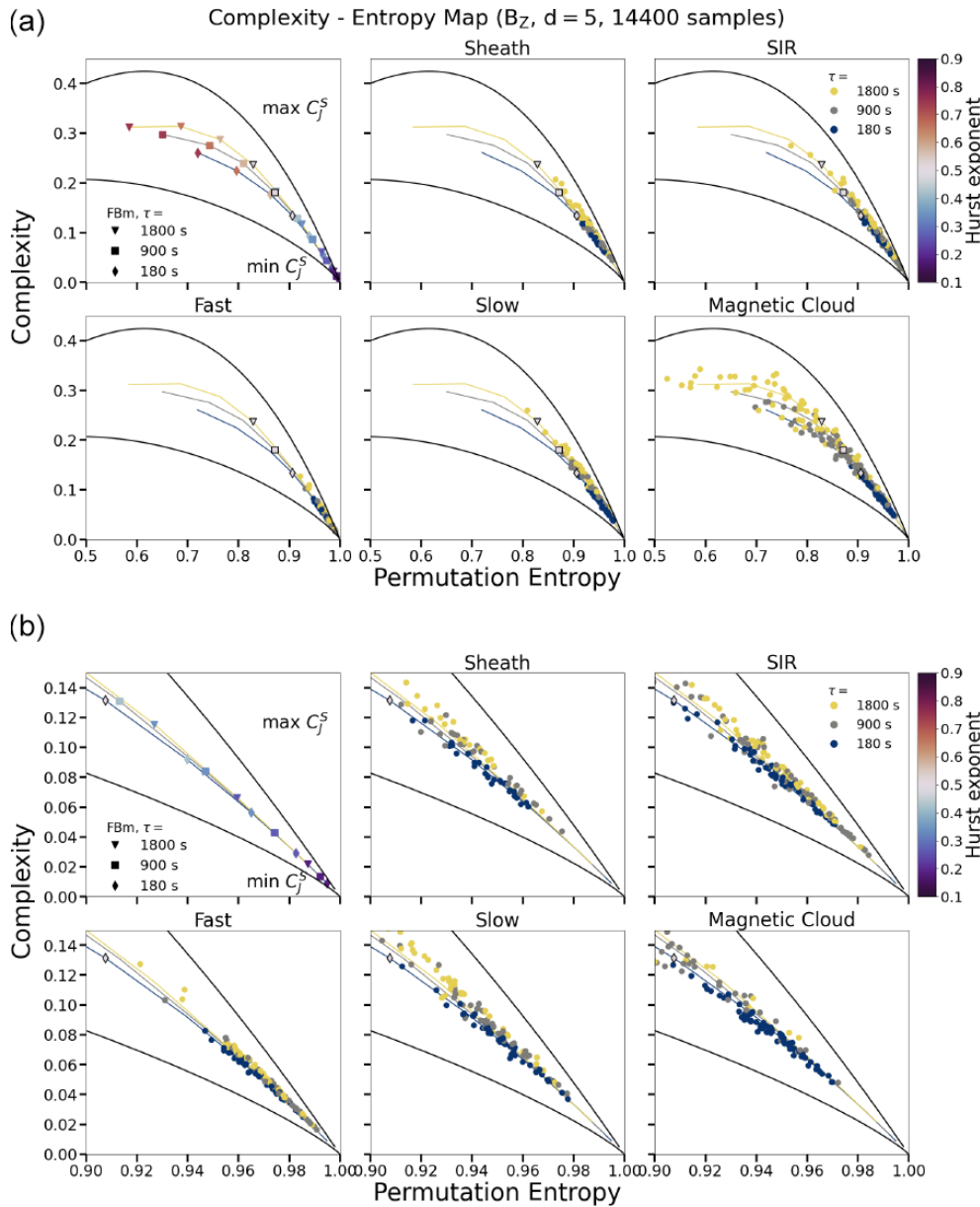


Figure 4. Complexity–entropy maps showing Jensen–Shannon complexity in B_Z plotted against normalised permutation entropy for $d = 5$ and subsampling rates ranging from $r = 20$ to 600 in steps of 60 ($\tau = 60$ to 1800 s in steps of 60 s). The dark-blue points show values for $r = 20$, with the point colour darkening to yellow with increasing r . In panel (a), the grey square and diamond markers show the fractional Brownian motion calculated with $r = 20$ and $r = 600$, respectively, for Hurst exponents from 0.1 to 0.8. The markers repeated in all panels with black edges indicate $H = 0.5$. Minimum and maximum complexity curves are shown in black.

of τ for all other solar wind types except for magnetic clouds. For magnetic clouds, the entropy values strongly decreased, and complexity values strongly increased with increasing τ .

The entropy being approximately constant across the τ range with a slight increase towards the largest timescales is a signature of stochastic fluctuations (e.g. Osmane et al., 2019). This trend was identified here in particular for the fast wind that also had, throughout the investigated τ range, the highest entropy and lowest complexity values. These find-

ings imply that the fast wind is the most stochastic in nature out of all the investigated solar wind types. This finding is consistent with the fast streams having high Alfvénicity due to the frequent presence of stochastic Alfvénic fluctuations propagating through the wind (e.g. Belcher and Davis, 1971; Bruno and Carbone, 2013).

The above-described entropy and complexity trends found for magnetic clouds are, in turn, in agreement with our understanding of magnetic clouds as ordered structures featur-

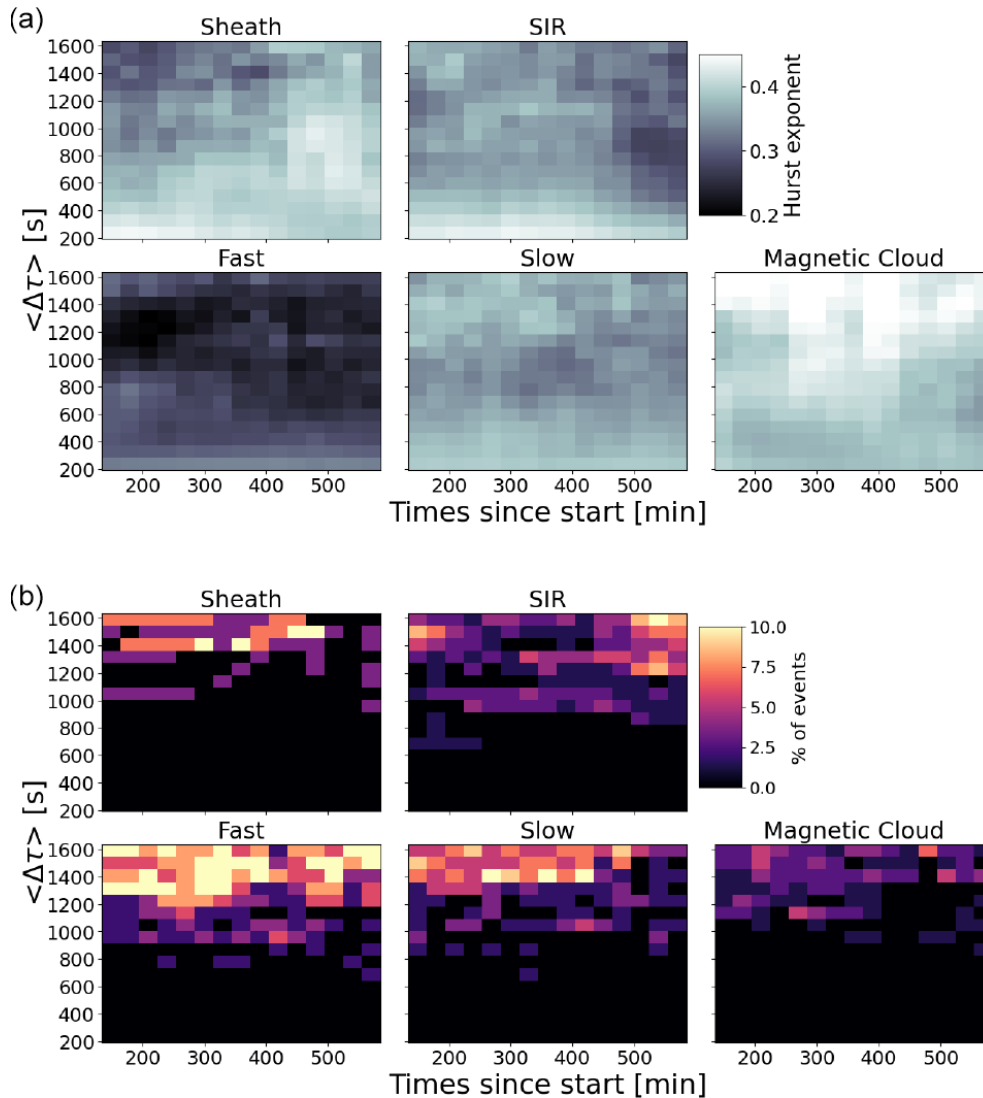


Figure 5. (a) Colour maps showing the values of the local Hurst exponent as a function of time (given in minutes from the start of the solar wind time interval) and the mid-point of the time lag interval used to calculate the Hurst exponent (see text for details). (b) The percentage of the events for which the standard error related to the fitting was > 0.05 . These events were removed from the analysis.

ing low magnetic field variability and smooth rotation of the field direction over an interval of 1 d (e.g. Klein and Burlaga, 1982; Kilpua et al., 2017a) and, as discussed above, strong bias toward ordinal patterns where the values were steadily increasing or decreasing. The analysis of *Ulysses* data by Raath et al. (2022) also suggested that parts of the low-entropy data periods in their study are associated with ordered magnetic clouds. The reason we found that, in magnetic clouds, B_Y and B_Z components show higher complexities at larger timescales than B_X is likely a reflection of the fact that the large-scale and coherent magnetic field rotation in them occurs predominantly in B_Y and B_Z . As mentioned earlier, their internal configuration is a magnetic flux rope. These structures propagate radially from the Sun; therefore, the minimum rotation of the field is in B_X .

Our finding that the fast wind had higher entropy and lower complexity than the slow wind is in contrast to Weygand and Kivelson (2019) but in agreement with Weck et al. (2015). The reason could be that Weygand and Kivelson (2019) used the *Ulysses* data at larger heliospheric distances, while our study and that of Weck et al. (2015) use *Wind* data gathered at 1 au. Fast wind is considered to be dynamically younger and is therefore expected to present less evolved turbulence (i.e. to be less stochastic) than slow wind (e.g. Weygand and Kivelson, 2019). However, it could be that, at least near 1 au, slow wind has considerably more coherent structures, while the fast wind is permeated by Alfvénic fluctuations, which are inherently stochastic in nature. The intermittency of the fast wind is, in fact, known to increase with heliospheric distance from the Sun, while for the slow wind, it remains ap-

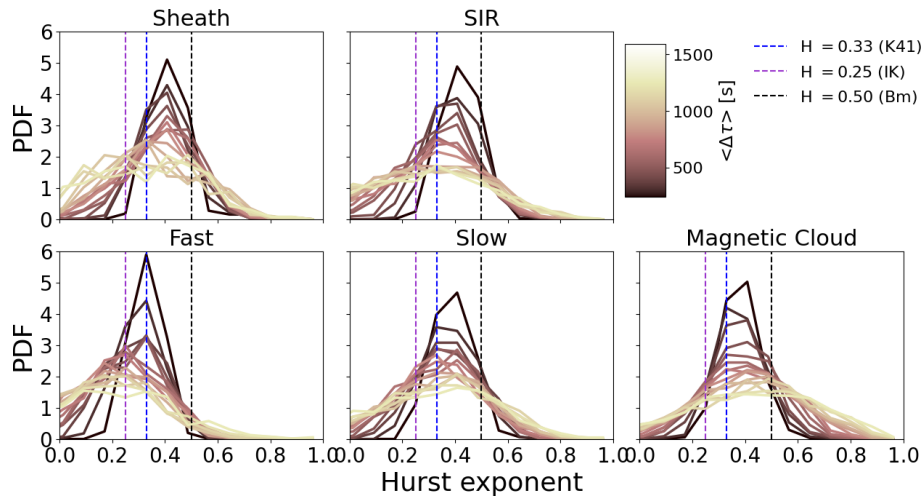


Figure 6. Probability density functions (PDFs) of the Hurst exponents calculated over varying time lag ranges for different solar wind types.

proximately the same (e.g. Marsch and Liu, 1993). We also note that Weygang and Kivelson (2019) found complexities and entropies in interplanetary CMEs (ICMEs) to be similar to those of the slow wind, while in our study, magnetic clouds had distinctly different values at larger time lags. We note that, in addition, with the inclusion of larger time lags, we separated sheaths from the ejecta and included only magnetic clouds that are the most coherent subset of ICMEs. Weygang and Kivelson (2019) included ICMEs as a whole, and they also included all ICMEs and not only magnetic clouds.

The placement of data points in the complexity–entropy plane indicates that, for most cases, solar wind fluctuations follow the fractional Brownian motion (fBm) curves relatively closely. At the smallest scales, the values fall exactly on the fBm curve, while at larger scales, there are some deviations, mostly above the fBm curve. This suggests higher ordering that likely stems from the presence of coherent structures such as current sheets, small-scale flux ropes and magnetic holes. These findings are consistent with previous studies that found solar wind fluctuations to be stochastic in nature, i.e. the absence of chaotic or periodic fluctuations (e.g. Weck et al., 2015; Weygang and Kivelson, 2019; Good et al., 2020; Kilpua et al., 2022). It is, however, possible that, if larger timescales would have been included, the most coherent magnetic clouds would have fallen into the periodic domain of the complexity–entropy plane as the time series of their magnetic field components resemble that of a half-wave.

The fast wind exhibits the least spread in its data points in the complexity–entropy plane, and they are clustered closest to the lower-right part of the map, close to the region where pink or white noise is located. This is in agreement with the previously discussed results of the entropy and complexity analysis, suggesting that the fast wind is highly stochastic in nature.

The widest spread of values in the complexity–entropy plane was observed for magnetic clouds for the largest time lags. This could partly stem from a large variety of magnetic cloud structures observed in interplanetary space, from those exhibiting distinctly smooth rotation to cases where considerable distortion is present (e.g. Kilpua et al., 2017a). However, for magnetic clouds, the data points at 180 s were also clustered close on the fBm curve, consistent with our previous suggestion of the uniformity of the processes at smaller scales in all solar wind types.

The relative similarity in terms of fluctuation properties and placement in the complexity–entropy plane for the slow wind and the large-scale compressive structures (sheaths and SIRs) could stem from the latter mostly consisting of the processed slow wind. Although, according to previous studies, fluctuation properties change from the upstream to downstream at ICME-driven shocks, with some new fluctuations being created, they do not appear to reset the turbulence in a similar manner to planetary bow shocks (Kilpua et al., 2021).

Both the entropy–complexity map analysis and PDFs of Hurst exponents derived from the first-order structure function analysis showed a wide spread of Hurst exponents for the investigated time series at the larger time lags. It is also interesting to note that, for all other investigated solar wind types, except for magnetic clouds, most data points reaching the lowest-right corner of the complexity–entropy map, i.e. data points associated with the lowest Hurst exponents, were related to $\tau = 900$ and 1800 s. In turn, all data points that were at the highest Hurst exponent values along the fBm curve were related almost solely to the largest time lag of 1800 s.

As discussed in Sect. 3.3 the Hurst exponent expresses whether fluctuations are persistent, random or anti-persistent. Both the complexity–entropy maps and the Hurst exponents obtained from the structure function analysis indicate dom-

inantly anti-persistent fluctuations ($H < 0.5$) for all investigated solar wind types and timescales.

The exponents extending to the persistent regime ($H > 0.5$) were identified mostly in magnetic clouds and for the largest timescales. Visually (Fig. 1), time series of the magnetic field components extracted during magnetic clouds resemble persistent time series with large Hurst exponents. We note that a significant fraction of magnetic clouds did, however, have Hurst exponents close to $H = 0.5$, i.e. being indicative of an uncorrelated random walk. Using the relation $\alpha = 2H + 1$, this corresponds to the inertial range spectral slope -2 , i.e. considerably steeper than Kolmogorov's. Recently, Good et al. (2023) showed that magnetic clouds in the inner heliosphere can indeed exhibit slopes as steep as -2 at large scales. Rather than a property of the fluctuations, Good et al. (2023) interpret these steep slopes as a feature of the background magnetic structure, with rotation of the global flux rope field in the clouds adding power to the spectra at large scales. However, we again caution against drawing strong conclusions about the relation between the Hurst exponent and spectral slopes due to the effect of multifractality.

We found significant locality for the Hurst exponents, in particular for compressive SIRs and sheath structures. For sheaths, the trailing part had larger Hurst exponents than the front part, while for SIRs, the trend is opposite. We note that Kilpua et al. (2021) also found differences in spectral slopes between the leading and trailing parts of the sheath. The larger Hurst exponents in the back of the sheath could stem from highly fluctuating and more compressive fields near the flux rope's leading edge. The draping of the field lines around the flux rope, reconnection and depletion regions can lead to current sheaths and discontinuities. For magnetic clouds, the larger Hurst exponents at the middle part of the cloud could stem from this region representing the least disturbed part of the structure. The boundaries of magnetic clouds are often distorted by their interaction with the ambient solar wind (e.g. Kilpua et al., 2013). We note that Balasis et al. (2006) found a change in the Hurst exponents for geomagnetic time series, going from anti-persistent to persistent properties preceding intense magnetospheric storms, i.e. before the occurrence of an extreme event. In our work, we analysed solar wind time series only within the large-scale structures, but it will be an interesting future work to extend the study to analyse the temporal variations in the scaling properties of continuous solar wind time series over longer periods.

5 Conclusions

In this work, we have characterised time series sampled in fast and slow wind, magnetic clouds, CME-driven sheaths, and SIRs. The time series were analysed by estimating their permutation entropy, Jensen–Shannon complexity and Hurst exponents from the first-order structure function. The re-

sults reflect different dynamical processes behind the generation and evolution of the solar wind structures and different behaviours with varying timescales. At small scales, all of the solar wind types show a similar occurrence frequency in terms of ordinal patterns, entropy and complexity values, while clear differences are evident at large scales. All solar wind types except magnetic clouds at the largest scales follow the fractional Brownian motion (fBm) relatively closely in the complexity–entropy plane but are partly located on different parts of the timescale-dependent fBm curve. The fast wind and magnetic clouds stood out as having the most distinct fluctuation characteristics, while the slow wind and compressive structures (SIRs and sheaths) resembled each other more closely. We also found a significant non-locality in Hurst exponents, in particular for sheaths and SIRs.

This study demonstrates that permutation entropy and complexity analysis is a useful tool for investigating the solar wind and its large-scale structures. The analysis can help to explore their internal processes and how these internal processes relate to the local fluctuation properties. In addition, the complexity–entropy analysis could reveal the occurrence of mesoscale structures in a statistical sense in space plasmas at different scales as they are expected to add more structures to the data, hence leading to higher complexity. Observations from the fleet of recently launched spacecraft (*Solar Orbiter*, *Parker Solar Probe* and *BepiColombo*) are also expected to yield important information on variations with heliospheric distances.

Data availability. The solar wind data used in this study are available from the NASA Goddard Space Flight Center Coordinated Data Analysis Web (CDAWeb; <http://cdaweb.gsfc.nasa.gov/>, Candey, 2024). The Wind ICME list is available at https://wind.nasa.gov/ICME_catalog/ (Nieves-Chinchilla, 2024), the Richardson and ICME lists are available at <https://izw1.caltech.edu/ACE/ASC/DATA/level3/icmetable2.htm> (Richardson and Cane, 2024; Richardson and Cane, 2010), and the ACE/WIND SIR catalogue is available at http://www.srl.caltech.edu/ACE/ASC/DATA/level3/SIR_List_1995_2009_Jian.pdf (Jian, 2024). The pink and white noise was generated using the code publicly available at <https://github.com/felixpatzelt/colorednoise> (Patzelt, 2024), and the fractional Brownian motion was generated with the package publicly available at <https://pypi.org/project/fbm/> (Flynn, 2024).

Author contributions. EKJK performed the data analysis and prepared the figures. All the authors have contributed to the writing of the paper and interpretation of the results.

Competing interests. The contact author has declared that none of the authors has any competing interests.

Disclaimer. Publisher's note: Copernicus Publications remains neutral with regard to jurisdictional claims made in the text, published maps, institutional affiliations, or any other geographical representation in this paper. While Copernicus Publications makes every effort to include appropriate place names, the final responsibility lies with the authors.

Acknowledgements. We acknowledge the Finnish Centre of Excellence in Research of Sustainable Space (Academy of Finland grant no. 312390). Emilia K. J. Kilpua acknowledges the ERC under the European Union's Horizon 2020 Research and Innovation Programme (project no. SolMAG 724391). Simon Good is supported by the Academy of Finland (grant nos. 338486 and 346612) (IN-ERTUM). Matti Ala-Lahti acknowledges the Emil Aaltonen Foundation for the financial support.

Financial support. The funding has been provided through the Academy of Finland (project nos. 312390, 338486 and 346612) and the European Union Horizon 2020 programme (project grant no. 724391).

Open-access funding was provided by the Helsinki University Library.

Review statement. This paper was edited by Peter Wurz and reviewed by three anonymous referees.

References

- Balasis, G., Daglis, I. A., Kapiris, P., Mandea, M., Vassiliadis, D., and Eftaxias, K.: From pre-storm activity to magnetic storms: a transition described in terms of fractal dynamics, *Ann. Geophys.*, 24, 3557–3567, <https://doi.org/10.5194/angeo-24-3557-2006>, 2006.
- Balasis, G., Balikhin, M. A., Chapman, S. C., Consolini, G., Daglis, I. A., Donner, R. V., Kurths, J., Paluš, M., Runge, J., Tsurutani, B. T., Vassiliadis, D., Wing, S., Gjerloev, J. W., Johnson, J., Matarassi, M., Alberti, T., Papadimitriou, C., Manshour, P., Boutsis, A. Z., and Stumpo, M.: Complex Systems Methods Characterizing Nonlinear Processes in the Near-Earth Electromagnetic Environment: Recent Advances and Open Challenges, *Space Sci. Rev.*, 219, 38, <https://doi.org/10.1007/s11214-023-00979-7>, 2023.
- Bandt, C. and Pompe, B.: Permutation Entropy: A Natural Complexity Measure for Time Series, *Phys. Rev. Lett.*, 88, 174102, <https://doi.org/10.1103/PhysRevLett.88.174102>, 2002.
- Belcher, J. W. and Davis, Leverett, J.: Large-amplitude Alfvén waves in the interplanetary medium, 2, *J. Geophys. Res.*, 76, 3534, <https://doi.org/10.1029/JA076i016p03534>, 1971.
- Borovsky, J. E. and Funsten, H. O.: Role of solar wind turbulence in the coupling of the solar wind to the Earth's magnetosphere, *J. Geophys. Res.*, 108, 1246, <https://doi.org/10.1029/2002JA009601>, 2003.
- Borovsky, J. E., Denton, M. H., and Smith, C. W.: Some Properties of the Solar Wind Turbulence at 1 AU Statistically Examined in the Different Types of Solar Wind Plasma, *J. Geophys. Res.-Space*, 124, 2406–2424, <https://doi.org/10.1029/2019JA026580>, 2019.
- Bruno, R.: Intermittency in Solar Wind Turbulence From Fluid to Kinetic Scales, *Earth Space Sci.*, 6, 656–672, <https://doi.org/10.1029/2018EA000535>, 2019.
- Bruno, R. and Carbone, V.: The Solar Wind as a Turbulence Laboratory, *Living Rev. Sol. Phys.*, 10, 2, <https://doi.org/10.12942/lrsp-2013-2>, 2013.
- Bruno, R., Carbone, V., Sorriso-Valvo, L., and Bavassano, B.: Radial evolution of solar wind intermittency in the inner heliosphere, *J. Geophys. Res.-Space*, 108, 1130, <https://doi.org/10.1029/2002JA009615>, 2003.
- Burlaga, L., Sittler, E., Mariani, F., and Schwenn, R.: Magnetic loop behind an interplanetary shock: Voyager, Helios, and IMP 8 observations, *J. Geophys. Res.*, 86, 6673–6684, <https://doi.org/10.1029/JA086iA08p06673>, 1981.
- Candey, R. M.: Coordinated Data Analysis Web, CDAWeb [data set], <https://cdaweb.gsfc.nasa.gov>, last access: 5 May 2024.
- Chen, C. H. K., Bale, S. D., Bonnell, J. W., Borovikov, D., Bowen, T. A., Burgess, D., Case, A. W., Chandran, B. D. G., de Wit, T. D., Goetz, K., Harvey, P. R., Kasper, J. C., Klein, K. G., Korrück, K. E., Larson, D., Livi, R., MacDowall, R. J., Malaspina, D. M., Mallet, A., McManus, M. D., Moncuquet, M., Pulupa, M., Stevens, M. L., and Whittlesey, P.: The Evolution and Role of Solar Wind Turbulence in the Inner Heliosphere, *Astrophys. J. Suppl. S.*, 246, 53, <https://doi.org/10.3847/1538-4365/ab60a3>, 2020.
- Dai, L., Han, Y., Wang, C., Yao, S., Gonzalez, W., Duan, S., Lavraud, B., Ren, Y., and Guo, Z.: Geoeffectiveness of Interplanetary Alfvén Waves, I. Magnetopause Magnetic Reconnection and Directly Driven Substorms, *Astrophys. J.*, 945, 47, <https://doi.org/10.3847/1538-4357/ab267>, 2023.
- De Michelis, P., Consolini, G., Tozzi, R., and Marcucci, M. F.: Observations of high-latitude geomagnetic field fluctuations during St. Patrick's Day storm: Swarm and SuperDARN measurements, *Earth Planet. Space*, 68, 105, <https://doi.org/10.1186/s40623-016-0476-3>, 2016.
- di Matteo, T.: Multi-scaling in finance, *Quant. Financ.*, 7, 21–36, <https://doi.org/10.1080/14697680600969727>, 2007.
- Flynn, C.: fbm 0.3.0 [data set], <https://pypi.org/project/fbm/>, last access: 5 May 2024.
- Giannattasio, F., Consolini, G., Berrilli, F., and De Michelis, P.: Scaling properties of magnetic field fluctuations in the quiet Sun, *Astron. Astrophys.*, 659, A180, <https://doi.org/10.1051/0004-6361/202142940>, 2022.
- Gilmore, M., Yu, C. X., Rhodes, T. L., and Peebles, W. A.: Investigation of rescaled range analysis, the Hurst exponent, and long-time correlations in plasma turbulence, *Phys. Plasmas*, 9, 1312–1317, <https://doi.org/10.1063/1.1459707>, 2002.
- Gomes, L. F., Gomes, T. F. P., Rempel, E. L., and Gama, S.: Origin of multifractality in solar wind turbulence: the role of current sheets, *Mon. Not. R. Astron. Soc.*, 519, 3623–3634, <https://doi.org/10.1093/mnras/stac3577>, 2023.
- Good, S. W., Ala-Lahti, M., Palmerio, E., Kilpua, E. K. J., and Osmane, A.: Radial Evolution of Magnetic Field Fluctuations in an Interplanetary Coronal Mass Ejection Sheath, *Astron. Astrophys.*, 893, 110, <https://doi.org/10.3847/1538-4357/ab7fa2>, 2020.

- Good, S. W., Rantala, O. K., Jylhä, A. S. M., Chen, C. H. K., Möstl, C., and Kilpua, E. K. J.: Turbulence Properties of Interplanetary Coronal Mass Ejections in the Inner Heliosphere: Dependence on Proton Beta and Flux Rope Structure, *Astrophys. J. Lett.*, 956, <https://doi.org/10.3847/2041-8213/acfd1c>, 2023.
- Gosling, J. T., Asbridge, J. R., Bame, S. J., and Feldman, W. C.: Solar wind stream interfaces, *J. Geophys. Res.*, 83, 1401–1412, <https://doi.org/10.1029/JA083iA04p01401>, 1978.
- Han, Y., Dai, L., Yao, S., Wang, C., Gonzalez, W., Duan, S., Lavraud, B., Ren, Y., and Guo, Z.: Geoeffectiveness of Interplanetary Alfvén Waves, II. Spectral Characteristics and Geomagnetic Responses, *Astron. Astrophys.*, 945, 48, <https://doi.org/10.3847/1538-4357/acb266>, 2023.
- Iroshnikov, P. S.: Turbulence of a Conducting Fluid in a Strong Magnetic Field, *Soviet Astron.*, 7, p. 566, <https://ui.adsabs.harvard.edu/abs/1964SvA.....7..566I> (last access: 5 May 2024), 1964.
- Jian, L.: Stream Interaction Regions (SIRs) from Wind and ACE Data during 1995–2009 [data set], http://www.srl.caltech.edu/ACE/ASC/DATA/level3/SIR_List_1995_2009_Jian.pdf, last access: 5 May 2024.
- Jian, L., Russell, C. T., Luhmann, J. G., and Skoug, R. M.: Properties of Stream Interactions at One AU During 1995–2004, *Sol. Phys.*, 239, 337–392, <https://doi.org/10.1007/s11207-006-0132-3>, 2006.
- Kilpua, E., Koskinen, H. E. J., and Pulkkinen, T. I.: Coronal mass ejections and their sheath regions in interplanetary space, *Liv. Rev. Sol. Phys.*, 14, 5, <https://doi.org/10.1007/s41116-017-0009-6>, 2017a.
- Kilpua, E. K. J., Isavnin, A., Vourlidas, A., Koskinen, H. E. J., and Rodriguez, L.: On the relationship between interplanetary coronal mass ejections and magnetic clouds, *Ann. Geophys.*, 31, 1251–1265, <https://doi.org/10.5194/angeo-31-1251-2013>, 2013.
- Kilpua, E. K. J., Balogh, A., von Steiger, R., and Liu, Y. D.: Geoeffective Properties of Solar Transients and Stream Interaction Regions, *Space Sci. Rev.*, 212, 1271–1314, <https://doi.org/10.1007/s11214-017-0411-3>, 2017b.
- Kilpua, E. K. J., Fontaine, D., Good, S. W., Ala-Lahti, M., Osmane, A., Palmerio, E., Yordanova, E., Moissard, C., Hadid, L. Z., and Janvier, M.: Magnetic field fluctuation properties of coronal mass ejection-driven sheath regions in the near-Earth solar wind, *Ann. Geophys.*, 38, 999–1017, <https://doi.org/10.5194/angeo-38-999-2020>, 2020.
- Kilpua, E. K. J., Good, S. W., Ala-Lahti, M., Osmane, A., Fontaine, D., Hadid, L., Janvier, M., and Yordanova, E.: Statistical analysis of magnetic field fluctuations in CME-driven sheath regions, *Front. Astron. Space Sci.*, 7, 610278, <https://doi.org/10.3389/fspas.2020.610278>, 2021.
- Kilpua, E. K. J., Good, S. W., Ala-Lahti, M., Osmane, A., Pal, S., Soljento, J. E., Zhao, L. L., and Bale, S.: Structure and fluctuations of a slow ICME sheath observed at 0.5 au by the Parker Solar Probe, *Astron. Astrophys.*, 663, A108, <https://doi.org/10.1051/0004-6361/202142191>, 2022.
- Klein, L. W. and Burlaga, L. F.: Interplanetary magnetic clouds at 1 AU, *J. Geophys. Res.*, 87, 613–624, <https://doi.org/10.1029/JA087iA02p00613>, 1982.
- Kolmogorov, A.: The Local Structure of Turbulence in Incompressible Viscous Fluid for Very Large Reynolds' Numbers, *Akademiia Nauk SSSR Doklady*, 30, 301–305, 1941.
- Kraichnan, R. H.: Inertial-Range Spectrum of Hydro-magnetic Turbulence, *Phys. Fluids*, 8, 1385–1387, <https://doi.org/10.1063/1.1761412>, 1965.
- Lepping, R. P., Acuña, M. H., Burlaga, L. F., Farrell, W. M., Slavin, J. A., Schatten, K. H., Mariani, F., Ness, N. F., Neubauer, F. M., Whang, Y. C., Byrnes, J. B., Kennon, R. S., Panetta, P. V., Scheifele, J., and Worley, E. M.: The Wind Magnetic Field Investigation, *Space Sci. Rev.*, 71, 207–229, <https://doi.org/10.1007/BF00751330>, 1995.
- Mandelbrot, B. B.: The fractal geometry of nature, W. H. Freeman and Co., ISBN: 0716711869, 1977.
- Marsch, E. and Liu, S.: Structure functions and intermittency of velocity fluctuations in the inner solar wind, *Ann. Geophys.*, 11, 227–238, 1993.
- Marsch, E. and Tu, C.-Y.: Intermittency, non-Gaussian statistics and fractal scaling of MHD fluctuations in the solar wind, *Nonlin. Processes Geophys.*, 4, 101–124, <https://doi.org/10.5194/npg-4-101-1997>, 1997.
- Nieves-Chinchilla, T.: Wind ICME Catalogue 1995–2021, NASA [data set], https://wind.nasa.gov/ICME_catalog/, last access: 5 May 2024.
- Nieves-Chinchilla, T., Vourlidas, A., Raymond, J. C., Linton, M. G., Al-haddad, N., Savani, N. P., Szabo, A., and Hidalgo, M. A.: Understanding the Internal Magnetic Field Configurations of ICMEs Using More than 20 Years of Wind Observations, *Sol. Phys.*, 293, 25, <https://doi.org/10.1007/s11207-018-1247-z>, 2018.
- Ogilvie, K. W., Chornay, D. J., Fritzenreiter, R. J., Hunsaker, F., Keller, J., Lobell, J., Miller, G., Scudder, J. D., Sittler, E. C., J., Torbert, R. B., Bodet, D., Needell, G., Lazarus, A. J., Steinberg, J. T., Tappan, J. H., Mavretic, A., and Gergin, E.: SWE, A Comprehensive Plasma Instrument for the Wind Spacecraft, *Space Sci. Rev.*, 71, 55–77, <https://doi.org/10.1007/BF00751326>, 1995.
- Olivier, C. P., Engelbrecht, N. E., and Strauss, R. D.: Permutation Entropy Analysis of Magnetic Field Turbulence at 1 AU Revisited, *J. Geophys. Res.-Space*, 124, 4–18, <https://doi.org/10.1029/2018JA026102>, 2019.
- Osmane, A., Dimmock, A. P., Naderpour, R., Pulkkinen, T. I., and Nykyri, K.: The impact of solar wind ULF B_z fluctuations on geomagnetic activity for viscous timescales during strongly northward and southward IMF, *J. Geophys. Res.-Space*, 120, 9307–9322, <https://doi.org/10.1002/2015JA021505>, 2015.
- Osmane, A., Dimmock, A. P., and Pulkkinen, T. I.: Jensen-Shannon Complexity and Permutation Entropy Analysis of Geomagnetic Auroral Currents, *J. Geophys. Res.-Space*, 124, 2541–2551, <https://doi.org/10.1029/2018JA026248>, 2019.
- Oughton, S. and Engelbrecht, N. E.: Solar wind turbulence: Connections with energetic particles, *New Astron.*, 83, 101507, <https://doi.org/10.1016/j.newast.2020.101507>, 2021.
- Patzelt, F.: colorednoise.py, Github [data set], <https://github.com/felixpatzelt/colorednoise>, last access: 5 May 2024.
- Raath, J. L., Olivier, C. P., and Engelbrecht, N. E.: A Permutation Entropy Analysis of Voyager Interplanetary Magnetic Field Observations, *J. Geophys. Res.-Space*, 127, e30200, <https://doi.org/10.1029/2021JA030200>, 2022.
- Richardson, I. G.: Solar wind stream interaction regions throughout the heliosphere, *Liv. Rev. Sol. Phys.*, 15, 1, <https://doi.org/10.1007/s41116-017-0011-z>, 2018.

- Richardson, I. G. and Cane, H. V.: Near-Earth Interplanetary Coronal Mass Ejections During Solar Cycle 23 (1996–2009): Catalog and Summary of Properties, *Sol. Phys.*, 264, 189–237, <https://doi.org/10.1007/s11207-010-9568-6>, 2010.
- Richardson, I. G. and Cane, H. V.: Near-Earth Interplanetary Coronal Mass Ejections Since January 1996 [data set], <https://izw1.caltech.edu/ACE/ASC/DATA/level3/icmetable2.htm>, last access: 5 May 2024.
- Rosso, O. A., Zunino, L., Pérez, D. G., Figliola, A., Larrondo, H. A., Garavaglia, M., Martín, M. T., and Plastino, A.: Extracting features of Gaussian self-similar stochastic processes via the Bandt-Pompe approach, *Phys. Rev. E*, 76, 061114, <https://doi.org/10.1103/PhysRevE.76.061114>, 2007.
- Ruzmaikin, A., Feynman, J., and Robinson, P.: Long-term persistence of solar activity, *Sol. Phys.*, 149, 395–403, <https://doi.org/10.1007/BF00690625>, 1994.
- Smith, C. W. and Vasquez, B. J.: Driving and Dissipation of Solar-Wind Turbulence: What Is the Evidence?, *Front. Astron. Space Sci.*, 7, 611909, <https://doi.org/10.3389/fspas.2020.611909>, 2021.
- Telloni, D., D’Amicis, R., Bruno, R., Perrone, D., Sorriso-Valvo, L., Raghav, A. N., and Choraghe, K.: Alfvénicity-related Long Recovery Phases of Geomagnetic Storms: A Space Weather Perspective, *Astron. Astrophys.*, 916, 64, <https://doi.org/10.3847/1538-4357/ac071f>, 2021.
- Teodorescu, E., Echim, M., Munteanu, C., Zhang, T., Bruno, R., and Kovacs, P.: Inertial Range Turbulence of Fast and Slow Solar Wind at 0.72 AU and Solar Minimum, *Astrophys. J. Lett.*, 804, L41, <https://doi.org/10.1088/2041-8205/804/2/L41>, 2015.
- Viall, N. M., DeForest, C. E., and Kepko, L.: Mesoscale Structure in the Solar Wind, *Front. Astron. Space Sci.*, 8, 735034, <https://doi.org/10.3389/fspas.2021.735034>, 2021.
- Wawrzaszek, A. and Echim, M.: On the variation of intermittency of fast and slow solar wind with radial Distance, heliospheric Latitude, and Solar Cycle, *Front. Astron. Space Sci.*, 7, 617113, <https://doi.org/10.3389/fspas.2020.617113>, 2021.
- Weck, P. J., Schaffner, D. A., Brown, M. R., and Wicks, R. T.: Permutation entropy and statistical complexity analysis of turbulence in laboratory plasmas and the solar wind, *Phys. Rev. E*, 91, 023101, <https://doi.org/10.1103/PhysRevE.91.023101>, 2015.
- Weygand, J. M. and Kivelson, M. G.: Jensen-Shannon Complexity Measurements in Solar Wind Magnetic Field Fluctuations, *Astron. Astrophys.*, 872, 59, <https://doi.org/10.3847/1538-4357/aafda4>, 2019.
- Yordanova, E., Balogh, A., Noullez, A., and von Steiger, R.: Turbulence and intermittency in the heliospheric magnetic field in fast and slow solar wind, *J. Geophys. Res.-Space*, 114, A08101, <https://doi.org/10.1029/2009JA014067>, 2009.
- Zanin, M. and Olivares, F.: Ordinal patterns-based methodologies for distinguishing chaos from noise in discrete time series, *Commun. Phys.*, 4, 190, <https://doi.org/10.1038/s42005-021-00696-z>, 2021.